crystals

MDPI

Article

Effects of 147 MeV Kr Ions on the Structural, Optical and Luminescent Properties of $Gd_3Ga_5O_{12}$

Zhakyp T. Karipbayev [1,*], Gulnara M. Aralbayeva [1], Kuat K. Kumarbekov [1,*], Askhat B. Kakimov [1], Amangeldy M. Zhunusbekov [1], Abdirash Akilbekov [1], Mikhail G. Brik [2,3,4,5,6], Marina Konuhova [7], Sergii Ubizskii [8], Yevheniia Smortsova [9], Yana Suchikova [10], Snežana Djurković [3], Sergei Piskunov [7,*] and Anatoli I. Popov [1,7]

1 Department of Technical Physics, Institute of Physics and Technology, L.N. Gumilyov Eurasian National University, Kazhymukan St. 13, Astana 010008, Kazakhstan; aralbayeva_gm_1@enu.kz (G.M.A.); kakimov_ab_3@enu.kz (A.B.K.); zhunusbekov_am@enu.kz (A.M.Z.); akilbekov_at@enu.kz (A.A.); popov@latnet.lv (A.I.P.)
2 School of Integrated Circuits & CQUPT-BUL Innovation Institute, Chongqing University of Posts and Telecommunications, Chongqing 400065, China; mikhail.brik@ut.ee
3 Centre of Excellence for Photoconversion, Vinča Institute of Nuclear Sciences—National Institute of the Republic of Serbia, University of Belgrade, 11351 Belgrade, Serbia; snezana.djurkovic@vin.bg.ac.rs
4 Faculty of Science and Technology, Jan Długosz University, 42200 Częstochowa, Poland
5 Institute of Physics, University of Tartu, W. Ostwald Str. 1, 50411 Tartu, Estonia
6 Academy of Romanian Scientists, 3 Ilfov, 050044 Bucharest, Romania
7 Institute of Solid State Physics, University of Latvia, Kengaraga 8, Street, LV-1063 Riga, Latvia; marina.konuhova@cfi.lu.lv
8 Semiconductor Electronics Department, Lviv Polytechnic National University, S. Bandera Str. 12, 79013 Lviv, Ukraine; sergii.b.ubizskii@lpnu.ua
9 Deutsches Elektronen-Synchrotron (DESY), 22603 Hamburg, Germany; yevheniia.smortsova@desy.de
10 Scientific Department, Berdyansk State Pedagogical University, 69061 Zaporizhzhia, Ukraine; yanasuchikova@gmail.com
* Correspondence: karipbayev_zht_1@enu.kz (Z.T.K.); kumarbekov_kk_1@enu.kz (K.K.K.); piskunov@lu.lv (S.P.)

Abstract

The optical and vibrational responses of $Gd_3Ga_5O_{12}$ (GGG) single crystals to 147 MeV Kr-ion irradiations were systematically investigated to clarify defect formation pathways and their influence on luminescence mechanisms. Absorption spectra measured at room temperature reveal a stepwise redshift of the fundamental edge and the progressive development of a broad sub-band-gap tail between 4.4 and 5.3 eV, indicating the accumulation of F- and F^+-type oxygen-vacancy centers and increasing structural disorder. Raman spectroscopy shows that, despite substantial track overlap at fluences up to 10^{14} ions/cm^2, the crystal preserves its phonon frequencies and linewidths, while peak intensities decrease due to a growing disordered volume fraction. Low-temperature (13 K) photoluminescence demonstrates the persistence of a dominant broad band near 2.4 eV and the emergence of an additional irradiation-induced band at ~2.75 eV whose width increases with fluence, reflecting the formation of vacancy-related defect complexes. Excitation spectra transform from band-edge-dominated behavior in the pristine crystal to defect-tail-mediated excitation in heavily irradiated samples. These results provide a consistent spectroscopic picture of ion-track-induced disorder in GGG and identify the defect states governing its luminescence under extreme irradiation conditions.

Keywords: $Gd_3Ga_5O_{12}$ single crystals; luminescence; F centers; defects; Raman; scintillation materials

Academic Editor: Youngpak Lee

Received: 4 December 2025
Revised: 31 December 2025
Accepted: 31 December 2025
Published: 3 January 2026

1. Introduction

Gadolinium gallium garnet ($Gd_3Ga_5O_{12}$, GGG) is a cubic oxide (Ia3d) typically obtained as high-quality single crystals and widely used as a substrate for epitaxial optical and magneto-optical films [1–4]. Its wide band-gap (Eg ≈ 5.6 eV) and broad IR-UV transparency define its importance for photonic applications [3]. Rare-earth doping enables efficient phosphor and scintillation behavior: in Ce:GGG, emission and decay kinetics depend on the local crystal environment [5–7], while Er^{3+}-, Pr^{3+}- and Dy^{3+}-doped systems show characteristic f-f transitions [8,9]. Sol–gel approaches and isovalent substitutions support low-temperature phosphor synthesis [10]. Mechanical surface properties crucial for optical performance have been studied using nanoscratch and nanoindentation techniques [11–13], and Co diffusion has been linked to color-center formation [14].

In nanostructured and thin-film forms, GGG exhibits additional functionalities: GGG:Tb^{3+} and GGG:Eu^{3+} nanoparticles show stable and pressure-sensitive luminescence [15–17], while liquid-phase-epitaxial films operate in fast scintillators [18,19]. GGG has also been suggested as a wide-band-gap ceramic electrolyte for low-temperature fuel cells [20]. Cr^{3+} doping provides stable thermometric behavior, and Ca/Si substitutions in Cr:GGG adjust emission wavelength and decay time [21,22]. In Ce:GGG, the relative position of the Ce^{3+} $5d^1$ level to the conduction band and shallow traps has been determined, clarifying competition between radiative and trapping channels [23].

GGG is further recognized as a frustrated magnetic system exhibiting field-induced phase transitions and an enhanced magnetocaloric response upon Al incorporation [24–27]. The crystal also demonstrates remarkable radiation tolerance, including reversible amorphization-recrystallization cycles [28], radiation-induced absorption and Raman changes under neutron and heavy-ion exposure [29–32], and ion-track formation behavior consistent with the inelastic thermal-spike model [33–36]. Its similarity to the radiation response of the YIG garnet matrix confirms the generality of structural disordering and recovery mechanisms across garnets [37,38]. Exceptional mechanical robustness and thermal resistance have been verified under dynamic compression up to 2.6 TPa [39].

The role of defect- and trap-related states in determining the optical response of garnets is evident in both doped and nominally pure systems [40]. In Ce-containing alumino-gallate garnets $Gd_3Ga_3Al_2O_{12}$:Ce, thermally stimulated relaxation over a broad temperature range (~80–550 K) is governed by electron traps with characteristic depths of ~1.20 eV (Eu^{3+}) and ~0.76 eV (Yb^{3+}) and frequency factors on the order of ~10^{11} s^{-1}, indicating that the defect-trap reservoir controls excitation-energy redistribution and the balance between radiative and non-radiative processes [40]. In structurally disordered solid solutions based on $Gd_3Ga_5O_{12}$–$Gd_3Al_5O_{12}$, low-temperature (T < 6 K) absorption and luminescence spectra show that local symmetry and disorder are directly reflected in the linewidths, energies, and multiplicity of rare-earth 0–0 lines, demonstrating the key role of the local microscopic environment in excitation transfer [41]. Consistently, irradiation of GGG with swift heavy ^{131}Xe ions (231 MeV) leads to mesoscopic defect accumulation manifested by Raman-line broadening (FWHM increase of ~20–100%) and a reduction of microhardness down to ~60% of the initial value at fluences of 1×10^{11}–3.3×10^{13} ions/cm^2, evidencing progressive structural relaxation and disordering in the near-surface region [42].

Intrinsic defect-related luminescence in garnets is mainly governed by oxygen-vacancy centers—F (V_O with two electrons) and F^+ (V_O with one electron)—together with self-trapped and defect-localized excitons (STE/LE). In YAG [43] and LuAG [44], a fast violet band near ~3.1–3.2 eV (τ ≈ 2–3 ns), excited at ~3.3/5.3/6.5 eV, is attributed to F^+ centers, whereas a blue-green band around ~2.6–2.7 eV is associated with F centers [43–45]. Antisite disorder (Y_{Al}/Lu_{Al}) enhances the formation of F^+-antisite complexes, shifting and broaden-

ing these emissions and partially suppressing STE; both F and F^+ can also be excited from the excitonic continuum (~6.5–7.3 eV) [43–45].

In mixed garnets such as GAGG:Ce, as well as in YAG, exposure to swift heavy ions produces persistent photo-induced absorption across the UV–visible range and strongly weakens VUV–exciton emission, indicating an increased population of F-type defects and stronger competition with Ce^{3+} 5d-4f radiative channels, potentially involving Ce^{3+}/Ce^{4+} charge conversion [46,47]. For sintered garnets, parameters such as oxygen partial pressure, grain boundaries, and impurity–defect complexes enhance F/F^+ luminescence and suppress STE, whereas oxidative annealing decreases color-center concentrations—critical for optical and scintillation performance.

Ionoluminescence of a $Y_3Al_5O_{12}:Ce^{3+}$ single crystal under irradiation with 2 MeV H^+ ions shows that changes in the luminescence characteristics are significantly weaker than those induced by temperature [48]. A comparison of fluence- and temperature-dependent effects indicates that heating is the primary factor responsible for the reduction of Ce^{3+} emission intensity and the red shift of the band, whereas proton irradiation contributes only a limited effect.

The previous study [33] demonstrated that irradiation of GGG with 147 MeV ^{84}Kr ions causes a ~30 nm red shift of the absorption edge, an increase in oxygen-vacancy concentration, lattice expansion, and pronounced ion-track softening, all indicating the formation of track-induced disorder and F-type defect centers. The present work is a logical continuation of that study and extends the fluence range to 10^{11}, 10^{12}, 10^{13}, and 10^{14} ion/cm^2, enabling a step-by-step analysis of defect evolution. The aim is to establish the relationship between structural disorder and changes in optical and luminescent properties, identify defect levels, and clarify their influence on sub-band-gap absorption, excitation pathways, and low-temperature defect luminescence.

2. Materials and Methods

Single crystals of GGG were produced by the Czochralski technique in an iridium crucible under a mildly oxidizing atmosphere at the SRC "Electron-Carat" (Lviv, Ukraine) [33]. The growth was carried out in an atmosphere composed of 98% Ar and 2% O_2. High-purity Gd_2O_3 and Ga_2O_3 powders (99.99 wt%) served as the starting reagents. It is known that tetravalent impurities such as Si^{4+} and Zr^{4+} in the raw materials can introduce cation vacancies and stimulate spiral growth in rare-earth gallium garnets. To minimize these effects, a small amount of CaO (10^{-2}–10^{-3} wt%) was added to the melt. GGG crystals typically contain trace levels (10^{-3}–10^{-4} wt%) of unintentional impurities, which are nearly impossible to eliminate during crystal growth. For this study, the samples were cut into flat plates 0.48 mm thick, oriented along the (111) crystallographic plane, and double-sided polished to optical-grade finish.

The GGG crystal samples were irradiated at 300 K with Kr^{+15} ions at an energy of 1.75 MeV per nucleon at fluences of 1×10^{11}, 1×10^{12}, 1×10^{13}, 5×10^{13}, and 1×10^{14} ions/cm^2 using the DC-60 heavy-ion accelerator(The Institute of Nuclear Physics, Astana, Kazakhstan) at the Institute of Nuclear Physics in Astana, Kazakhstan. The ion beam current was in the range of 25–30 nA/cm^2. Note that, in recent years, this accelerator has been widely and successfully employed in studies of point and extended defects across a broad range of materials [49–58].

Raman spectra were recorded using a TriVista 777 triple grating spectrometer (Princeton Instruments, Trento, USA)and a 532 nm (3.63 mW) laser at room temperature (RT).

Luminescence spectroscopy was performed under synchrotron excitation. Excitation and emission spectra were obtained at the FinEstBeAMS undulator beamline [59–65] at the MAX IV 1.5 GeV storage ring (Lund, Sweden). The photon energy used for excitation

ranged from 4.5 to 11.0 eV. Emission in the 200–700 nm UV–visible region was analyzed using an Andor Shamrock SR-303i monochromator (Andor Technology, Belfast, UK) (0.3 m) coupled to a Newton DU970P-BVF CCD detector (Andor Technology, Belfast, UK), enabling detection across 200–900 nm. The GGG crystals (ELECTRON-CARAT SCIENTIFIC-RESEARCH COMPANY, Lviv, Ukraine)were installed on the cold finger of a closed-cycle cryostat (Advanced Research Systems) housed in an ultra-high-vacuum chamber with a base pressure of ~10^{-9} mbar.

Additional luminescence experiments at 9 K were carried out using synchrotron radiation at the Superlumi P66 beamline (PETRA III, DESY) [66]. Excitation was selected with a 2 m monochromator providing a 4 Å spectral resolution. The emitted light was analyzed using an ANDOR Kymera monochromator(Andor Technology, Belfast, UK) (2 Å resolution) equipped with a CCD camera and a Hamamatsu R6358 photomultiplier. Excitation spectra were calibrated using sodium salicylate to ensure accurate spectral response.

3. Results and Discussion

3.1. Absorption Spectra Analysis

The absorption spectra (Figure 1) of GGG irradiated with 147 MeV Kr ions exhibit a pronounced fluence-dependent red shift of the optical edge accompanied by a systematic increase in sub-band-gap absorption. In the pristine crystal, the absorption edge is sharp and located near 220 nm; below 300 nm, only narrow Gd^{3+} 4f-4f transitions and a weak absorption band in the 280–400 nm range, attributed to Ca^{2+}-V_O complexes, are observed [30].

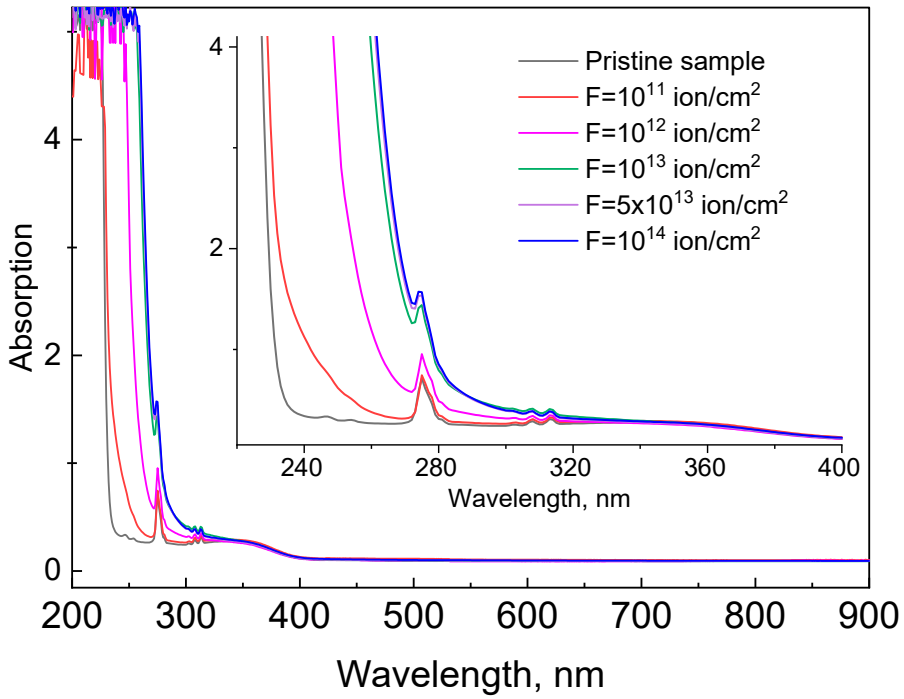

Figure 1. Absorption spectra of GGG single crystals at RT.

At a fluence of 10^{11} ions/cm^2, the absorption edge becomes less steep and shifts to approximately 230 nm, while a distinct absorption tail develops between 230 and 300 nm, indicating the formation of initial oxygen vacancies and F/F^+ centers introducing localized states into the band gap [30,33]. With increasing fluence to 10^{12} ions/cm^2, the edge shifts further to ~235–240 nm, and the defect-related band near ~280 nm increases significantly in intensity.

For fluences of 10^{13} and 5×10^{13} ions/cm^2, the absorption spectra nearly overlap: the edge stabilizes at 240–245 nm, and a broad defect-related absorption band develops

in the 240–320 nm region. In this regime, the narrow Gd^{3+} absorption lines are partially obscured by the growing defect background, although weak features at 254, 275, and 313 nm can still be discerned and are assigned to the intra-configurational 4f-4f transitions of Gd^{3+} ($^8S_{7/2} \rightarrow {}^6D_J$, ^6I_J, and ^6P_J, respectively) [30,33]. Their apparent weakening is therefore not related to changes in the electronic structure of Gd^{3+} ions, but to the superposition of an increasingly strong sub-band-gap absorption associated with oxygen-vacancy-related defects.

At the highest fluence of 10^{14} ions/cm^2, the position of the absorption edge remains nearly unchanged, while the sub-band-gap absorption reaches its maximum: the 230–320 nm region transforms into an almost continuous background, and the Gd^{3+} 4f-4f lines appear only as slight modulations. Overall, the observed stepwise redshift of the absorption edge and the monotonic growth of defect-related absorption are governed by the accumulation and clustering of F/F^+ centers and their impurity-related complexes, whereas the intrinsic Gd^{3+} spectral pattern remains preserved throughout the entire fluence range.

The spectral extent and maximum of the sub-band-gap absorption are determined by the density and energetic distribution of oxygen-vacancy-related defect states (F and F^+ centers) within the band gap. At low defect concentrations, these states are located close to the conduction-band minimum, resulting in a weak absorption tail. With increasing defect accumulation and clustering, the absorption extends deeper into the band gap. The initial level of sub-band-gap absorption is influenced by growth-related defects introduced during synthesis; however, at higher irradiation fluences, the absorption behavior is dominated by irradiation-induced vacancies and becomes largely independent of the initial defect concentration.

3.2. Raman Spectra Analysis

Raman spectroscopy data for GGG irradiated with 147 MeV Kr ions demonstrate that, up to fluences of 1×10^{14} ions/cm^2, the crystal remains predominantly crystalline and does not undergo track-induced amorphization of the type reported for several garnets such as YIG [38].

In the pristine sample, a characteristic GGG set of Raman lines is observed at ~112, 171, 181, 240, 261, 274, 355, 382, 525, 583, 598, 741, and 888 cm^{-1}, corresponding to 13 out of 25 group theoretically allowed modes [30,37,38] (A_{1g}, E_g, T_{2g}) (Figure 2). Their symmetry and atomic displacements agree well with calculations and prior measurements [27,30,37,67–69] for $(Gd,Y)_3Ga_5O_{12}$: the low-frequency modes (≈100–300 cm^{-1}) reflect translational–rotational motions of GdO_8 dodecahedra and collective GdO_8-GaO_6-GaO_4 vibrations, whereas the bands at 525–740 cm^{-1} originate from internal bending and stretching modes of GaO_4 and GaO_6 polyhedra (Table 1).

Comparison of peak positions and widths (FWHM) in pristine and irradiated samples shows that the frequencies of the principal modes remain essentially unchanged: the shifts do not exceed 0.2–0.3 cm^{-1}, which is within the experimental uncertainty and far below the ~1–2 cm^{-1} shifts observed under intense neutron irradiation of GGG up to 10^{18} n/cm^2 [30]. Line widths—3–6 cm^{-1} for low-frequency and 10–17 cm^{-1} for high-frequency modes—also remain almost constant across the fluence range 1×10^{13}–1×10^{14} ions/cm^2. This indicates that local symmetry and the character of interatomic bonding in GaO_6 and GaO_4 units remain largely unaffected: the lifetimes of optical phonons and the distribution of local force constants do not change. Unlike neutron irradiation, dominated by displacement cascades and statistical accumulation of point defects—which leads to noticeable phonon "softening" and line broadening—swift-heavy-ion damage is governed by electronic stopping and the associated thermal spike confined to narrow cylindrical tracks.

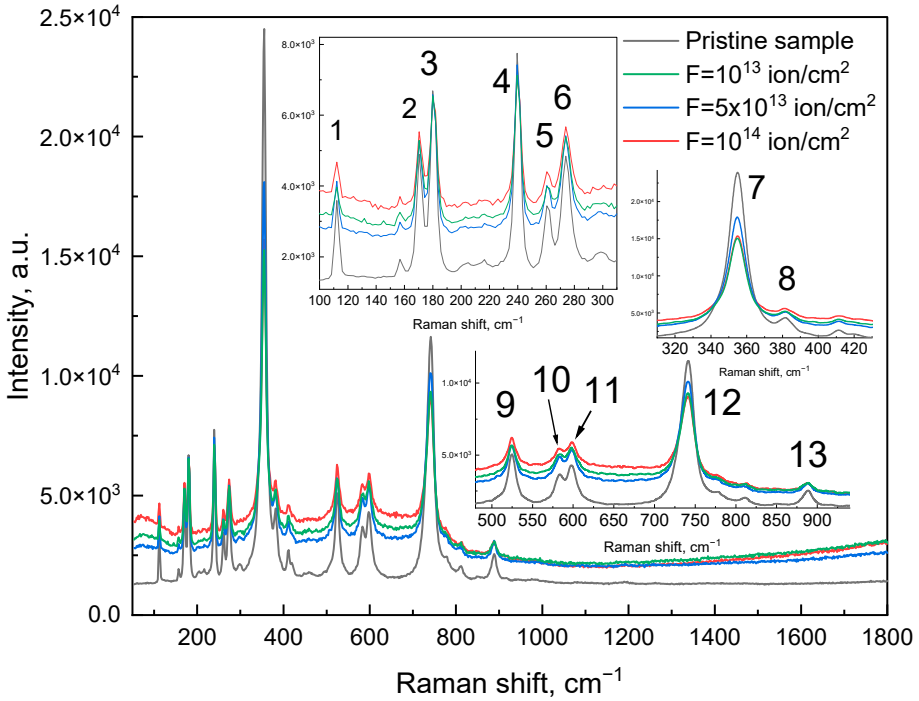

Figure 2. Raman spectra of pristine and Kr ion irradiated with 147 MeV energy GGG single crystals by various fluences.

Table 1. Raman spectra peak positions and FWHM of pristine and Kr ion irradiated with 147 MeV energy GGG single crystals by various fluences and comparison with [30,37,38] the literature.

No	Raman Modes	This Work								Unirradiated Sample [37]	Au 12 MeV, [38]	Neutron Irradiated [30]	
		Pristine Sample		$F = 10^{13}$ ion/cm^2		$F = 5 \times 10^{13}$ ion/cm^2		$F = 10^{14}$ ion/cm^2					
		ν, cm^{-1}	FWHM, cm^{-1}	ν, cm^{-1}	FWHM, cm^{-1}	ν, cm^{-1}	FWHM, cm^{-1}	ν, cm^{-1}	FWHM, cm^{-1}		$F = 3 \times 10^{14}$	$F = 10^{16}$ n/cm^2	$F = 10^{18}$ n/cm^2
1	E_g	112.3	3.9	112.2	3.5	112.0	4.0	112.4	0.0	110.0	110.9	111.5	110.6
2	T_{2g}	170.6	4.5	170.6	4.2	170.4	4.7	170.2	1.4	170.0	171.9	169.7	169.6
3	T_{2g}	180.6	4.3	180.6	4.2	180.5	4.5	180.3	1.5	180.0	180.2	179.3	179.4
4	T_{2g}	239.9	4.2	239.9	4.1	239.9	4.3	239.6	1.5	239.0	241.3	239.0	238.4
5	E_g	261.3	3.3	261.4	3.2	261.3	2.7	260.7	1.2	261.0	260.3	260.7	260.2
6	T_{2g}	274.1	6.2	274.0	5.6	274.0	6.0	274.0	2.1	273.0	274.6	273.5	273.1
7	A_{1g}	354.8	10.9	354.7	11.1	354.6	11.2	355.3	3.7	353.0	353.5	353.9	354.8
8	T_{2g}	382.0	6.5	381.8	5.9	382.0	6.4	380.9	3.5	381.0	380.0	379.8	379.5
9	T_{2g}	524.6	10.8	524.6	9.5	524.4	10.4	524.8	3.4	524.0	525.6	524.6	523.8
10	A_{1g}	582.9	10.1	583.2	9.7	582.9	9.9	583.0	3.6	583.0	585.4	584.1	582.9
11	T_{2g}	598.3	12.9	598.3	11.9	598.4	12.6	599.1	3.8	598.0	596.2	598.6	598.4
12	T_{2g}	740.6	16.9	740.5	15.8	740.3	16.2	741.5	5.3	740.0	740.8	741.6	741.2
13	T_{2g}	888.3	12.3	888.0	11.8	888.3	12.3	887.5	3.5	858/896	896.1	–	–

The most sensitive quantities are not frequency or linewidth but integral peak intensities and the level of the incoherent background. According to the first document, as the fluence increases to 1×10^{14} ions/cm^2, the integrated intensities of all Raman peaks decrease by roughly a factor of two, while a broad background grows in the high-frequency region. This behavior is naturally interpreted within a partial track-amorphization model. Each 147 MeV Kr ion loses energy mainly via ionization; thermal-spike calculations and data for related garnets such as YIG show that, once the electronic stopping exceeds ~4 MeV/μm, a cylindrical amorphous or strongly disordered core forms [36–38]. The radius of such a core in garnets is several nanometers. At fluences of 10^{13}–10^{14} ion/cm^2, the average distance between tracks becomes comparable to their diameters, although the volume fraction of the amorphous phase remains below ~50%.

Raman peaks arise from coherent vibrations of the periodic lattice. If the crystalline fraction in the laser-probed volume is (1-f) and the amorphous fraction is f, the integrated intensity of discrete modes scales as (1-f), whereas the incoherent background and density-of-states-like "pseudobands" scale roughly with f [34–38]. The observed twofold decrease at the highest fluence corresponds to f $\approx$ 0.5, i.e., about half of the probed volume is occupied by tracks and their overlap zones, while the remaining half remains crystalline and sustains the same phonon frequencies and linewidths. This explains the combination of nearly unchanged frequencies with reduced intensities and an increased background.

Correlating changes in different modes with specific structural units clarifies the distribution of damage across the sublattices. Low-frequency E_g (~112 cm^{-1}) and T_{2g} (~170–180 cm^{-1}) modes associated with GdO_8 dodecahedra decrease in intensity synchronously with the high-frequency GaO_4/GaO_6 modes. The absence of selective attenuation of any group of lines indicates that the electronic track perturbs the lattice uniformly, without preferential damage to either the cationic (Gd^{3+} vs. Ga^{3+} or anionic sublattice. This agrees with optical-absorption data: the ~30 nm redshift of the absorption edge in GGG after Kr-ion irradiation is attributed to an increase in lattice parameter and accumulation of disordered regions along tracks, not to selective disruption of a particular sublattice [33].

Comparison with Co ion diffusion studies in GGG [14] shows that both chemical doping and swift-ion irradiation produce similar Raman signatures: altered relative intensities of low- and high-frequency modes and increased background while preserving peak positions. This points to a shared mechanism—local symmetry breaking and perturbation of force-constant distributions without destruction of the global cubic structure. In both cases, lattice strain is predominantly local; the average cell parameter and mean bond lengths change only weakly, consistent with the absence of systematic phonon softening seen, for example, in isovalent Gd→Y substitution in $(Gd_{1-x}Y_x)_3Ga_5O_{12}$ [67].

A comparison with more severe irradiation conditions in YIG highlights the high radiation tolerance of GGG. In $Y_3Fe_5O_{12}$, at fluences $\geq 10^{14}$ ion/cm^2, swift ions produce nearly complete lattice randomization, and the Raman spectrum collapses to two broad bands characteristic of amorphous materials [37]. In GGG, however, the full set of discrete lines persists at the same fluences, indicating that even with substantial track overlap, the amorphous phase does not become continuous. This is consistent with the modest softening and reduced nanohardness observed by nanoindentation, as well as with the moderate increase in lattice parameter measured by X-ray diffraction.

Thus, rigorous analysis of the Raman data supports the following physical picture. Kr ions with an energy of 147 MeV generate cylindrical regions of intense electronic excitation in GGG. Each ion impact forms a narrow track with a highly disordered core and a partially relaxed periphery. At fluences up to 10^{13} ions/cm^2 the tracks barely overlap, the amorphous volume fraction is small, and the Raman spectrum remains nearly identical to that of the pristine crystal. At 5×10^{13} and 1×10^{14} ions/cm^2, track overlap forms an interconnected network of disordered regions, reducing the effective volume of coherently vibrating lattice and increasing the incoherent background; however, the crystalline matrix retains its original symmetry and local vibrational dynamics. A full transition to the amorphous-like state observed in irradiated YIG does not occur under the present conditions; GGG exhibits robust preservation of its phonon spectrum and, consequently, high structural radiation tolerance.

3.3. Luminescence Spectra

The luminescence spectra of GGG at T $\approx$ 13 K under 5 eV SR photon excitation show (Figure 3) that even the pristine, unirradiated crystal already contains a significant population of defect-related centers. The dominant emission is a broad band with a

maximum near 2.4 eV, upon which narrow lines from unintentional impurities—Tb^{3+} lines at 3.25, 2.95, 2.82, 2.62, 2.28, 2.13 and 1.97 eV—correspond to $^5D_3/^5D_4 \rightarrow {}^7F_J$ transitions. The ~1.7 eV band is attributed to Cr^{3+} centers, while the weak ~1.6 eV feature is most probably related to unintentional Fe impurities [70,71], together with characteristic Gd^{3+} lines, including the transition at 317.4 nm (≈3.9 eV). Thus, GGG is not an ideal crystal initially; it contains intrinsic structural defects formed during growth as well as rare-earth impurity ions, both of which participate in the redistribution of excitation energy. As the irradiation fluence increases, the emission from these unintentional impurities is strongly quenched due to charge-state conversion. The broad-band emission is presumably associated with F and F^+ centers [72].

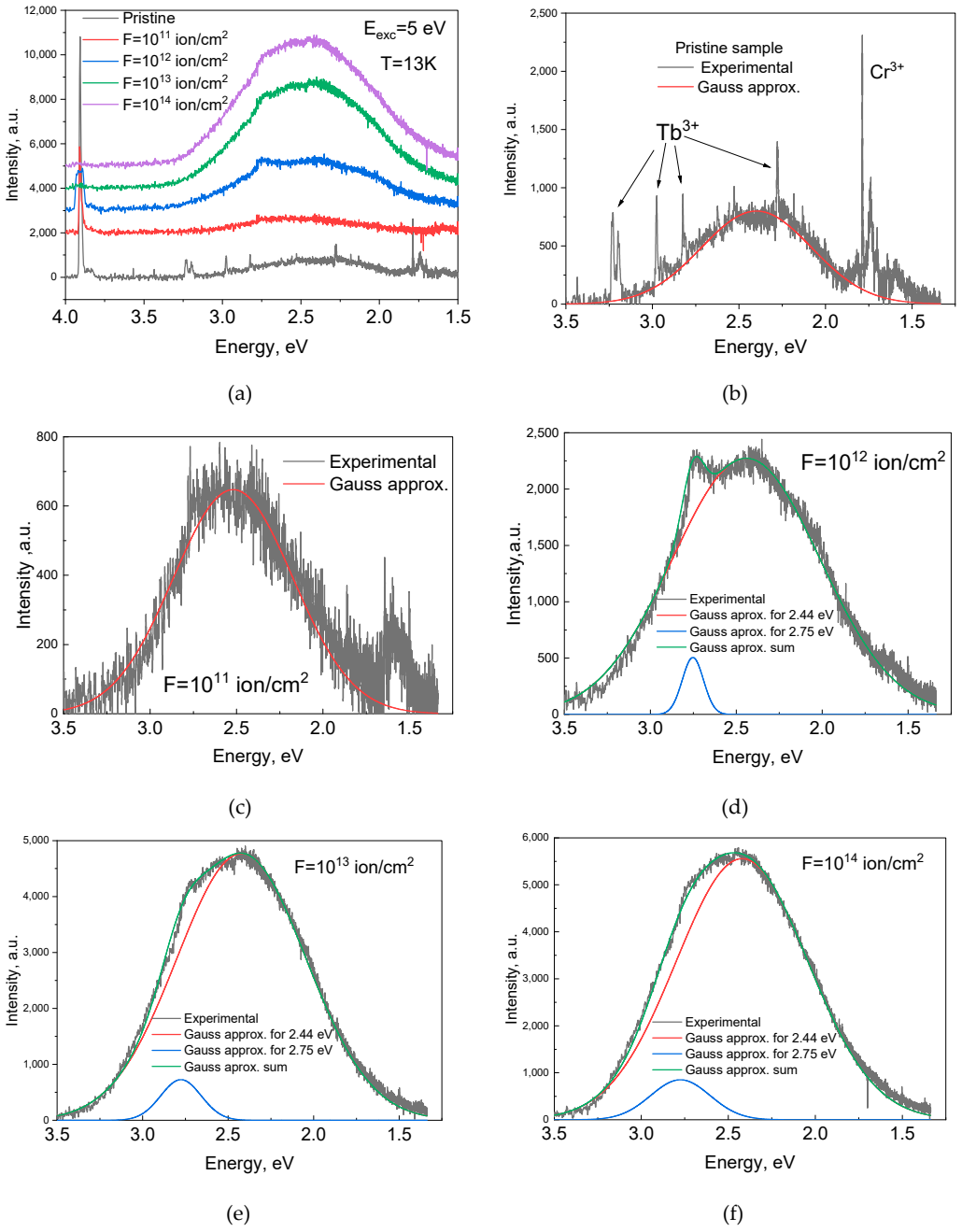

Figure 3. Luminescence spectra at T = 13 K of the initial crystal and crystals irradiated with krypton ions with an energy of 147 MeV, with different fluences, when excited by photons with an energy of 5 eV (**a**), Gaussian deconvolutions of the luminescence spectra of the initial crystal (**b**), irradiated with fluences of 10^{11} ion/cm^2 (**c**), 10^{12} ion/cm^2 (**d**), 10^{13} ion/cm^2 (**e**), 10^{14} ion/cm^2 (**f**).

Gaussian deconvolution (Table 2) of the spectra shows that all samples retain the same overall emission pattern: a broad band with a maximum at $E_1 \approx 2.4$–2.44 eV is present both in the pristine crystal and after irradiation at all fluences. When moving from the unirradiated sample to 10^{11} ions/cm^2, this band broadens markedly (its FWHM increases from ~0.75 to ~1.0 eV), reflecting an increase in structural disorder and in the distribution of local fields within the lattice, while the position of the maximum remains essentially unchanged. This indicates that the nature of the emitting centers responsible for the main band remains the same, but the statistical distribution of their local environments becomes more heterogeneous due to the formation of the first radiation defects.

Table 2. Spectral parameters of pristine and Kr ion-irradiated GGG single crystal at T = 13 K.

Fluence, ion/cm^2	E_1, eV	ΔE, eV	E_2, eV	ΔE, eV
Pristine	2.40	0.75		
10^{11}	2.44	1.00	2.75	0.12
10^{12}	2.44	1.00	2.75	0.15
10^{13}	2.42	0.89	2.78	0.28
10^{14}	2.41	0.92	2.74	0.42

A qualitatively new phenomenon emerges beginning at fluences around 10^{12} ions/cm^2: an additional band with a maximum at $E_2 \approx 2.75$ eV appears on the high-energy side of the principal emission band and is clearly resolved through Gaussian deconvolution. For fluences of 10^{12}–10^{14} ions/cm^2, its peak energy remains nearly constant (2.75–2.78 eV), while its FWHM increases monotonically—from ~0.12 eV at 10^{12} ions/cm^2 to ~0.40 eV at 10^{14} ions/cm^2. This evolution indicates that irradiation produces a new class of luminescent centers with a fixed emission energy but with an increasingly broad distribution of local configurations. At low doses, these centers are relatively homogeneous and well-defined, whereas at higher doses they evolve into a family of centers with similar but not identical local environments—for example, defect clusters, complexes involving oxygen vacancies, or antisite ions such as Gd occupying Ga sites. As the contribution of the 2.75 eV band increases, its relative intensity becomes comparable to that of the 2.4 eV band, causing the integrated maximum of the total emission to shift slightly toward higher energies, and the overall spectrum acquires a more symmetric, dome-like shape.

Analysis of the spectra at 13 K shows that irradiation with swift heavy ions does not change the fundamental type of the primary emitting center responsible for the ~2.4 eV band. Instead, irradiation enhances this emission by increasing the number of defects and simultaneously raising the degree of structural disorder. At fluences $\geq 10^{12}$ ions/cm^2, an additional class of radiation-induced centers with an emission maximum near 2.75 eV is formed in the crystal; their spectral weight and configurational heterogeneity increase monotonically with dose. The growth of the FWHM of this band, while its maximum energy remains nearly unchanged, serves as a direct indicator of the accumulation and progressive complexity of the defect subsystem in GGG under ion irradiation.

3.4. Luminescence Excitation Spectra

The excitation spectra recorded at 13 K demonstrate that luminescence in GGG is generated through the same absorbing states over the entire excitation-energy range, with particular emphasis on the emission band at 2.44 eV. For this band, the excitation curves are virtually identical in shape for both the pristine crystal and all irradiated samples, indicating a common excitation mechanism. In the pristine GGG sample, the excitation maximum of the 2.44 eV emission is located near the fundamental absorption edge at

~5.5–5.7 eV, while the intensity below this energy is negligible. This behavior reflects the absence of pronounced sub-band-gap absorption centers and shows that the population of the defect-related 2.44 eV emitting centers proceeds predominantly via excitation into band or excitonic states.

With increasing Kr-ion fluence, the excitation spectrum of the 2.44 eV band exhibits systematic changes. Already at a fluence of 10^{11} ions/cm^2, a noticeable background contribution emerges throughout the 4–10 eV region, manifested as an enhanced low-energy excitation tail extending down to ~4 eV and a shift of the effective excitation threshold toward lower energies. This indicates the formation of a broad distribution of radiation-induced defect states within the band gap, which efficiently absorb excitation energy and subsequently relax into the centers responsible for the 2.44 eV emission. These defect states are primarily associated with oxygen vacancies and distortions of the cation sublattice.

At higher fluences of 10^{12} and 10^{13} ions/cm^2, the sub-band-gap contribution becomes dominant for the 2.44 eV luminescence. The excitation spectra evolve into a wide band with a maximum at ~5.1–5.3 eV and a smooth, extended low-energy tail, while the sharp step at the pristine absorption edge becomes progressively blurred. At the highest fluence of 10^{14} ions/cm^2, nearly the entire 4–7(8) eV range transforms into a homogeneous excitation continuum, and the excitation behavior of the 2.44 eV band becomes indistinguishable from that of other emission channels. This unambiguously demonstrates that excitation of the 2.44 eV luminescence proceeds through a common defect-mediated manifold of states formed in the band gap as a result of swift heavy-ion irradiation.

The influence of radiation defects is especially pronounced in the excitation spectra of the narrow Gd^{3+} emission line at 3.9 eV (317.4 nm) (Figure 4b). In the pristine crystal, the spectra exhibit distinct, well-resolved 4f-4f transitions on a weak background, together with a sharp step at the absorption edge near E_g. With increasing fluence, the background beneath these lines increases dramatically, the absorption edge shifts to lower energies and becomes smeared, and the lines broaden slightly and partially merge into the continuum. Because the intensity of this line is sensitive to energy transfer from the host lattice to Gd^{3+} ions, degradation of its excitation spectrum can be regarded as a sensitive indicator of accumulated structural damage and altered relaxation pathways: a fraction of the excitation that, in the pristine crystal, is transferred to Gd^{3+} 4f states is intercepted by defect centers in the irradiated sample and redistributed into broad-band defect luminescence.

The excitation spectra are fully consistent with the picture derived from optical and quantum-chemical data for GGG. According to ellipsometry and transmission measurements, the fundamental absorption edge of GGG corresponds to a direct band gap of ≈5.66 eV and is associated primarily with O-2p → Ga/Gd-5d charge-transfer excitation [63]. Modern DFT calculations (especially those employing the mBJ potential) yield a similar band-gap magnitude and show that the valence band is dominated by oxygen 2p orbitals, whereas the conduction-band minimum is formed mainly by Gd- and Ga-5d states. Accounting for the 4f electrons of Gd introduces additional localized levels near the band edges but does not alter the overall characterization of GGG as a wide-band-gap dielectric [73].

The absorption spectrum of the pristine crystal displays a steep rise at 5.6–5.7 eV and a series of narrow Gd^{3+} 4f-4f lines around 3.9 eV, corresponding to the $^8S_{7/2} \rightarrow {}^6D$, ^6I, and ^6P transitions. This picture is reproduced in your excitation spectra as follows. For the defect-related emission in the 2.44 eV region (Figure 4a), all curves exhibit a sharp, well-defined maximum near E ≈ 5.6 eV, coinciding with the fundamental absorption edge. This indicates a mechanism of "electron-hole pair generation in the matrix → carrier capture at a defect → radiative recombination." A portion of the excitation at higher energies, 7–10 eV,

is associated with deeper charge-transfer transitions, O-2p → Ga/Gd-5d, which also lead to excited states that subsequently relax into the defect centers.

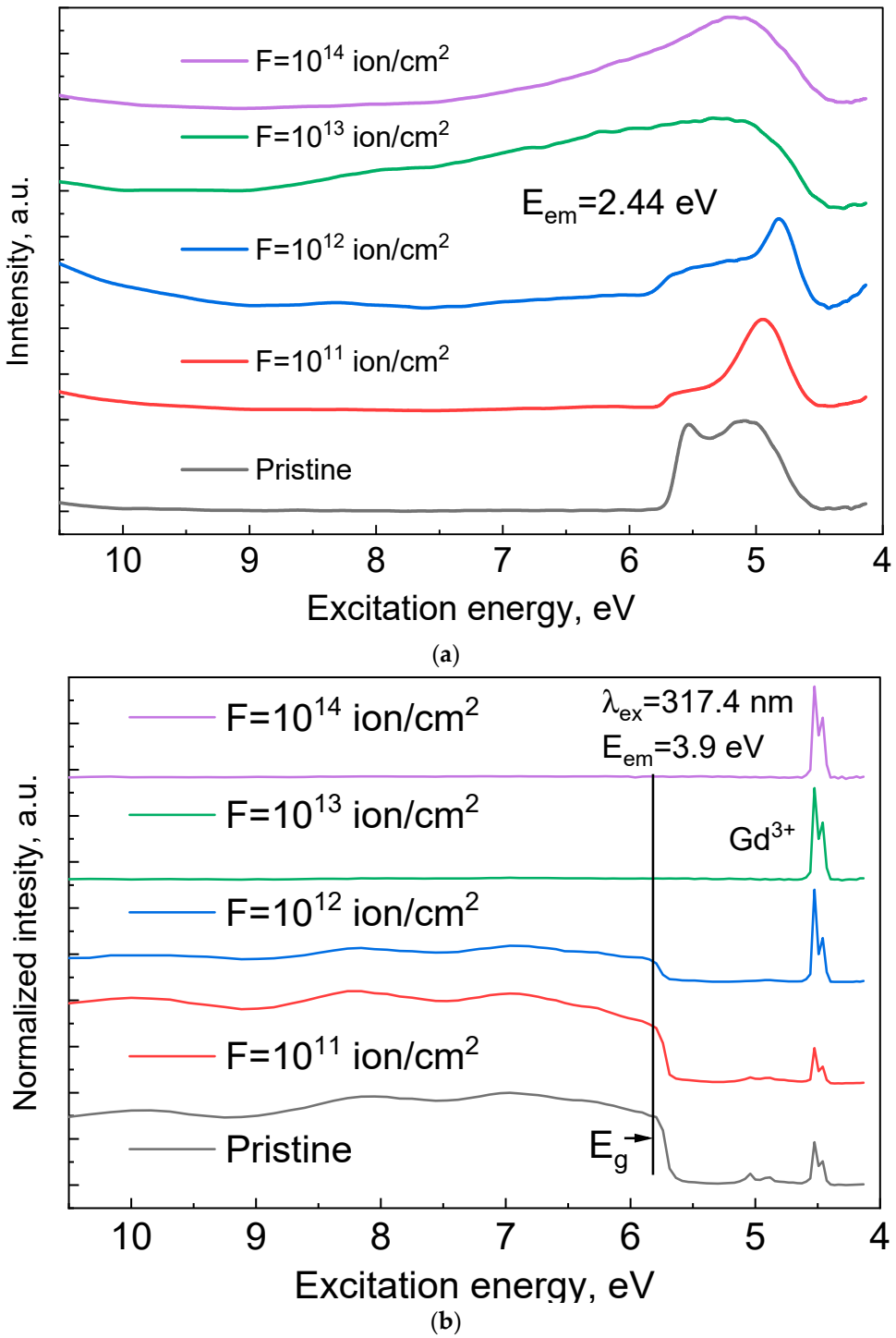

Figure 4. Luminescence excitation spectra at T = 13 K of the pristine and 147 MeV Kr ion-irradiated GGG single crystals for the initial crystal and at different fluences in the band of 2.44 eV (**a**) and at 3.9 eV (**b**).

Irradiation with 147 MeV Kr ions leads to a pronounced redistribution in the defect density and to shifts in the optical characteristics. According to absorption spectra, broad absorption bands associated with F-type centers (oxygen vacancies containing one or two electrons) and [F^+, Ca^{2+}] complexes become enhanced in the 280–350 nm region. Quantum-chemical modeling shows that the doubly charged oxygen vacancy [V_o^{2+}] in GGG does not

produce occupied states within the band gap and mainly shifts the Fermi level, whereas the neutral vacancy [V_o^0] generates localized states inside the gap, reducing transparency and opening new sub-band-gap excitation channels [73]. These defect levels lie roughly halfway between the valence-band maximum and the conduction-band minimum, consistent with the appearance of strong defect luminescence in the 2.4–2.8 eV region—that is, at ~3 eV below the conduction-band edge.

In the excitation spectra of the defect band with a maximum around 2.44 eV (Figure 4a), the pristine crystal shows a relatively narrow band slightly below 5.7 eV, located directly at the band edge. This corresponds to excitation via a free or weakly bound exciton followed by capture at existing structural defects. After irradiation to 10^{11} ions/cm^2, the band shape is essentially preserved, but as the fluence increases to 10^{13}–10^{14} ions/cm^2, the maximum noticeably broadens and shifts towards lower energies. This long-wavelength shift and broadening of the excitation band reflect two simultaneous effects: the development of an absorption tail due to band-edge smearing caused by microstrain and the introduction of oxygen vacancies, and additional transitions involving localized V_o^0 levels and their clusters located 0.3–0.6 eV below the conduction-band minimum. In DFT terms [73], this corresponds to the appearance of an additional mid-gap DOS band associated with two-electron vacancy states partially localized on nearby Gd ions (possibly forming Gd^{2+} via 4f-level occupation). As the fluence increases, the concentration of such centers rises, causing the excitation spectrum to evolve from a relatively narrow "edge-type" band into a broad continuum that reflects the distribution of local configurations within overlapping ion tracks.

3.5. Correlation Between Absorption (300 K) and Excitation Spectra (13 K)

The superimposed spectral curves clearly reveal the relationship between defect-related absorption and the excitation channels of luminescence (Figure 5). It is particularly important that the absorption spectra were measured at 300 K, whereas the excitation spectra of the 2.44 eV band were recorded at 13 K. In the pristine GGG single crystal (Figure 5a), the excitation maximum nearly coincides with the sharp fundamental absorption edge at ~5.5–5.6 eV; sub-band-gap absorption is weak, and therefore, at 13 K, defect luminescence is fed primarily by band-to-band or excitonic states generated upon absorption at room temperature.

With increasing fluence to 10^{11}–10^{12} ions/cm^2 (Figure 5b,c), the absorption edge measured at 300 K shifts to lower energies, and a pronounced tail emerges between ~5.5 and 4.5 eV. Against this background, the excitation maximum at 13 K broadens only slightly and shifts marginally toward lower energies: sub-band-gap transitions involving F and F^+ centers begin to contribute to the excitation of the defect band, although the dominant role of the band-edge excitation pathway is still preserved.

At higher fluences of 10^{13}–10^{14} ions/cm^2 (Figure 5d,e), the sub-band-gap tail becomes the dominant absorption feature; the 4.4–5.2 eV region is nearly filled by a continuous band, and further movement of the absorption edge essentially ceases (indicating saturation of the V_o concentration). The saturation of vacancy formation under ion irradiation occurs due to the balance between their creation, annihilation with interstitial atoms, and coalescence into defect clusters [74–80]. Correspondingly, the excitation maximum of the 2.44 eV band at 13 K broadens substantially and shifts to even lower energies. This behavior indicates that, in heavily irradiated GGG, the dominant excitation pathway for defect luminescence proceeds through the dense manifold of defect states forming the absorption tail, rather than through an idealized band-edge transition. Such a transition from excitonic/band-edge excitation to defect-tail excitation is fully consistent with the increasing concentration of F/F^+ centers and with the Raman spectroscopy evidence of track-induced disorder.

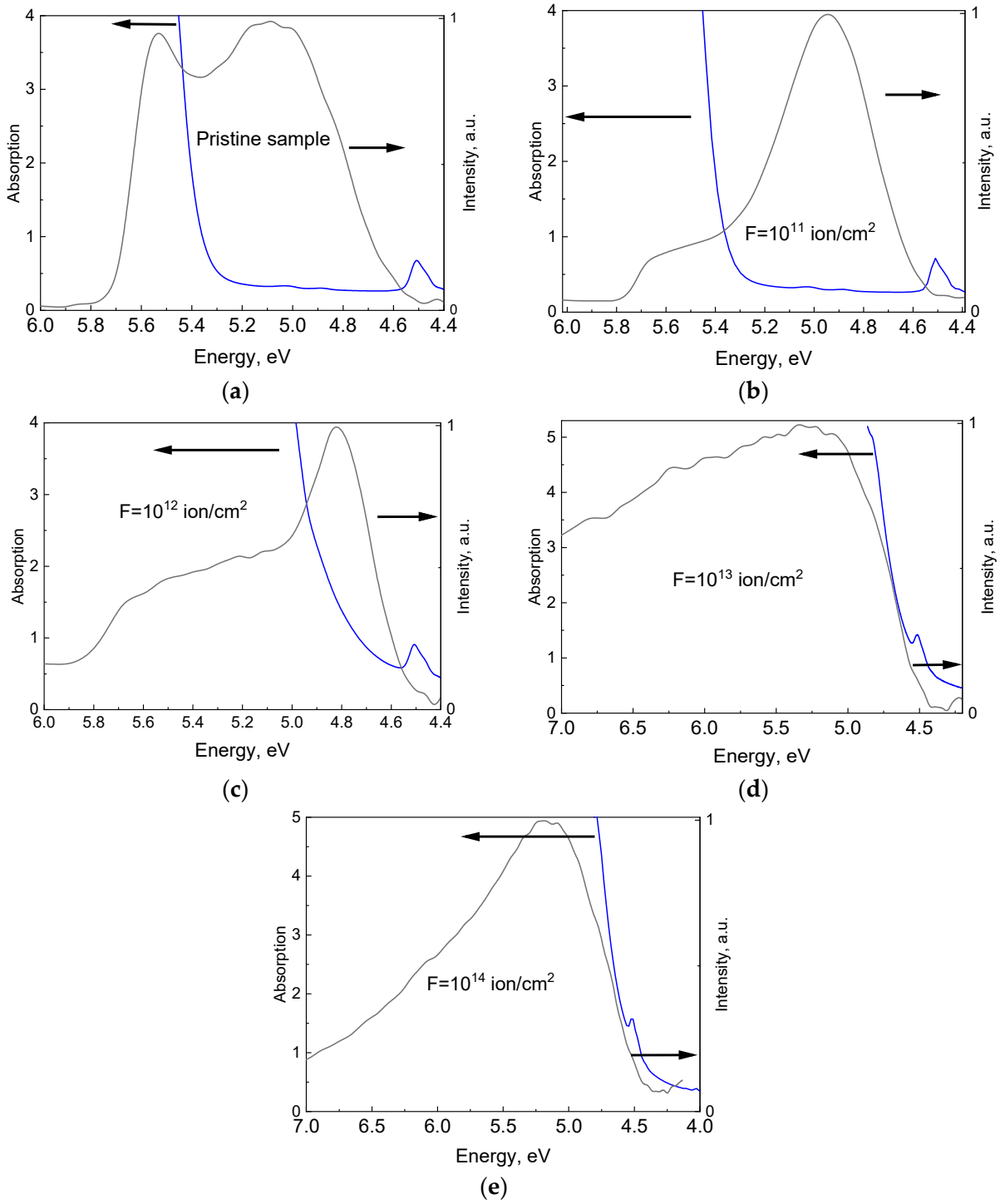

Figure 5. The luminescence excitation spectrum at 2.44 eV (T = 13 K), on the right along the ordinate and on the left along the ordinate, the absorption spectra (T = 300 K) of the pristine and 147 MeV Kr ion-irradiated GGG crystals with for (**a**)—pristine sample, (**b**)—10^{11} ion/cm^2, (**c**)—10^{12} ion/cm^2, (**d**)—10^{13} ion/cm^2, (**e**)—10^{14} ion/cm^2.

4. Conclusions

The comprehensive optical and vibrational analysis of GGG single crystals irradiated with 147 MeV Kr ions reveals a coherent picture of how swift heavy ions modify the defect landscape while preserving the fundamental structural integrity of the garnet lattice. Absorption measurements demonstrate a progressive redshift and broadening of the fundamental edge, together with the formation of a pronounced sub-band-gap tail,

indicating the accumulation of F- and F^+-type oxygen-vacancy centers and the emergence of defect-related band-tail states. Raman spectroscopy confirms that, even at the highest fluence of 10^{14} ions/cm^2, the lattice retains its phonon frequencies and linewidths, showing no signatures of full amorphization; instead, only the intensities of vibrational modes decrease, accompanied by an increased background that reflects partial overlap of ion tracks and the growth of a disordered volume fraction. Low-temperature luminescence reveals that the intrinsic broad emission near 2.4 eV remains the dominant radiative channel, while irradiation induces an additional band near 2.75 eV whose width increases systematically with fluence, signaling the formation of increasingly heterogeneous vacancy-related defect complexes. Excitation spectra further show a clear transformation from band-edge and excitonic excitation in the pristine crystal to defect-tail-mediated excitation in heavily irradiated samples, consistent with the absorption-edge smearing observed at room temperature. Altogether, these results demonstrate that high-energy Kr irradiation introduces a dense manifold of vacancy-type defect states that reshape excitation and emission pathways without destroying the crystalline symmetry of GGG, providing valuable insight into the mechanisms governing the optical resilience and radiation response of garnet-based scintillators and photonic materials.

Author Contributions: Conceptualization, A.A., M.G.B., S.U. and S.P.; data curation, Z.T.K., G.M.A., K.K.K., A.B.K., A.M.Z., M.K., Y.S. (Yevheniia Smortsova) and Y.S. (Yana Suchikova); formal analysis, A.M.Z., M.K., Y.S. (Yana Suchikova), S.D. and S.P.; funding acquisition, G.M.A.; investigation, M.G.B., Y.S. (Yana Suchikova) and S.P.; methodology, Z.T.K., A.A., M.G.B. and S.P.; project administration, G.M.A. and A.I.P.; resources, G.M.A., S.U., Y.S. (Yevheniia Smortsova) and A.I.P.; software, K.K.K., M.K., Y.S. (Yevheniia Smortsova) and S.D.; supervision, A.I.P.; validation, A.B.K., A.A. and S.U.; visualization, G.M.A., K.K.K., A.B.K. and S.D.; writing—original draft preparation, Z.T.K. and K.K.K.; writing—review and editing, Z.T.K., A.M.Z., M.G.B. and A.I.P. All authors have read and agreed to the published version of the manuscript.

Funding: This research was funded by the Science Committee of the Ministry of Science and Higher Education of the Republic of Kazakhstan (grant number AP19680626). In addition, Marina Konuhova and Anatoli I. Popov were supported by Latvian research project lzp-2023/1-0453, "Prediction of long-term stability of functional materials under extreme radiation conditions", and the Latvian State Research Program No. VPP-IZM-CERN-2022/1-0001.

Data Availability Statement: The raw data supporting the conclusions of this article will be made available by the authors upon reasonable request.

Acknowledgments: The authors acknowledge DESY (Hamburg, Germany), a member of the Helmholtz Association HGF, for providing experimental facilities. The work was carried out at the P66 beamline of PETRA III. Beamtime was allocated under proposal I-20250679 EC. The authors acknowledge MAX IV Laboratory for providing beamtime at the FinEstBeAMS beamline under Proposal 20231736.

Conflicts of Interest: The authors declare no conflicts of interest.

References

1. O'Kane, D.F.; Sadagopan, V.; Geiss, E.A.; Mandel, E. Crystal Growth and Characterization of Gadolinium Gallium Garnet. *J. Electrochem. Soc.* **1973**, *120*, 1272–1278. [CrossRef]
2. Xu, Y.-N.; Ching, W.Y.; Brickeen, B.K. Electronic structure and bonding in garnet crystals Electronic structure and bonding in garnet crystals $Gd_3Sc_2Ga_3O_{12}$, $Gd_3Sc_2Al_3O_{12}$, and $Gd_3Ga_3O_{12}$ compared to $Y_3Al_3O_{12}$. *Phys. Rev. B* **2000**, *61*, 1817. [CrossRef]
3. Ghimire, K.; Haneef, H.F.; Collins, R.W.; Podraza, N.J. Optical Properties of Single-Crystal $Gd_3Ga_5O_{12}$ from the Infrared to the Ultraviolet. *Phys. Status Solidi B* **2015**, *252*, 2191–2198. [CrossRef]
4. Zhao, G.; Li, T.; Xu, J. Growth of epitaxial substrate $Gd_3Ga_3O_{12}$ (GGG) single crystal through pure GGG phase polycrystalline material. *J. Cryst. Growth* **2002**, *237–239*, 720–724. [CrossRef]

5. Syvorotka, I.I.; Sugak, D.Y.; Wierzbicka, A.; Wittlin, A.; Przybylińska, H.; Barzowska, J.; Barcz, A.J.; Berkowski, M.; Domagała, J.Z.; Mahlik, S.; et al. Optical Properties of Pure and Ce^{3+}-Doped Gadolinium Gallium Garnet Crystals and Epitaxial Layers. *J. Lumin.* **2015**, *164*, 31–37. [CrossRef]
6. Mikhailov, M.M.; Neshchimenko, V.V.; Shavlyuk, V.V. The effects of binding type on luminescence LED phosphor based on GGG/Ce^{3+}. *Opt. Mater.* **2014**, *38*, 33–36. [CrossRef]
7. Thirumalaisamy, T.K.; Saravanakumar, S.; Butkute, S.; Kareiva, A.; Saravanan, R. Structure and Charge Density of Ce-Doped GGG. *J. Mater. Sci. Mater. Electron.* **2016**, *27*, 1920–1928. [CrossRef]
8. Wang, Y.; You, Z.; Li, J.; Zhu, Z.; Ma, E.; Tu, C. Spectroscopy of Highly Doped Er^{3+}:GGG and Er^{3+}/Pr^{3+}:GGG. *J. Phys. D Appl. Phys.* **2009**, *42*, 215406. [CrossRef]
9. Wang, Y.; You, Z.; Li, J.; Zhu, Z.; Tu, C. Optical Properties of Dy^{3+} in GGG. *J. Phys. D Appl. Phys.* **2010**, *43*, 075402. [CrossRef]
10. Butkute, S.; Zabiliute, A.; Skaudzius, R.; Zukauskas, A.; Kareiva, A. Sol-Gel Synthesis and Substitution in Ga-Garnets. *J. Sol-Gel Sci. Technol.* **2015**, *76*, 210–219. [CrossRef]
11. Li, C.; Zhang, F.; Meng, B.; Rao, X.; Zhou, Y. Research of material removal and deformation mechanism for single crystal GGG ($Gd_3Ga_5O_{12}$) based on varied-depth nanoscratch testing. *Mater. Des.* **2017**, *125*, 180–188. [CrossRef]
12. Li, C.; Zhang, F.; Wang, X.; Rao, X. Investigation on surface/subsurface deformation mechanism and mechanical properties of GGG single crystal induced by nanoindentation. *Appl. Opt.* **2018**, *57*, 3661–3668. [CrossRef]
13. Li, C.; Wu, Y.; Li, X.; Ma, L.; Zhang, F.; Huang, H. Deformation characteristics and surface generation modelling of crack-free grinding of GGG single crystals. *J. Mater. Process. Technol.* **2020**, *279*, 116577. [CrossRef]
14. Sugak, D.; Syvorotka, I.I.; Yakhnevych, U.; Buryy, O.; Vakiv, M.; Ubizskii, S.; Włodarczyk, D.; Zhydachevskyy, Y.; Pieniążek, A.; Jakiela, R.; et al. Investigation of Co Ions Diffusion in $Gd_3Ga_5O_{12}$ Single Crystals. *Acta Phys. Pol. A* **2018**, *133*, 959–964. [CrossRef]
15. Reshmi, C.P.; Ramesh, A.R.; Suresh, A.; Jaiswal-Nagar, D. Magnetic, magnetocaloric and optical properties of nano $Gd_3Ga_5O_{12}$garnet synthesized by citrate sol-gel method. *Int. J. Nano Dimens.* **2025**, *16*, 190–201. [CrossRef]
16. Luchechko, A.; Kostyk, L.; Varvarenko, S.; Tsvetkova, O.; Kravets, O. Green-Emitting $Gd_3Ga_5O_{12}$:Tb^{3+} Nanoparticles Phosphor: Synthesis, Structure, and Luminescence. *Nanoscale Res. Lett.* **2017**, *12*, 263. [CrossRef]
17. Jovanić, B.; Bettinelli, M.; Radenković, B.; Despotović-Zrakić, M.; Bogdanović, Z. Optical spectroscopy of nanocrystalline $Gd_3Ga_5O_{12}$ doped with Eu3+ and high pressures. *Mater. Chem. Phys.* **2012**, *132*, 273–277. [CrossRef]
18. Baillard, A.; Douissard, P.-A.; Loiko, P.; Martin, T.; Mathieu, E.; Camy, P. Terbium-doped gadolinium garnet thin films grown by liquid phase epitaxy for scintillation detectors. *RSC Adv.* **2025**, *15*, 20560–20568. [CrossRef]
19. Wollesen, L.; Douissard, P.-A.; Pauwels, K.; Baillard, A.; Loiko, P.; Brasse, G.; Mathieu, J.; Simeth, S.J.; Kratz, M.; Dujardin, C.; et al. Microstructured growth by liquid phase epitaxy of scintillating $Gd_3Ga_5O_{12}$(GGG) doped with Eu3+. *J. Alloys Compd.* **2025**, *1010*, 177267. [CrossRef]
20. Wang, K.; Xu, J.; Murakami, H.; Yamahara, H.; Seki, M.; Tabata, H.; Tonouchi, M. Terahertz Time-Domain Spectroscopy of Substituted Gadolinium Gallium Garnet. *Condens. Matter* **2025**, *10*, 1. [CrossRef]
21. Li, J.; Yousaf, M.; Ahmed, J.; Bibi, B.; Noor, A.; Alhokbany, N.; Sajid, M.; Nazar, A.; Shah, M.A.K.Y.; Guo, X.; et al. $Gd_3Ga_5O_{12}$: A wide bandgap semiconductor electrolyte for ceramic fuel cells, effective at temperatures below 500 C. *J. Rare Earths* **2025**, *43*, 2248–2256. [CrossRef]
22. Elzbieciak-Piecka, K.; Sójka, M.; Tian, F.; Li, J.; Zych, E.; Marciniak, L. The comparison of the thermometric performance of optical ceramics, microcrystals and nanocrystals of Cr^{3+}-doped $Gd_3Ga_5O_{12}$ garnets. *J. Alloys Compd.* **2023**, *963*, 171284. [CrossRef]
23. Shimoyama, N.; Kodama, S.; Bartosiewicz, K.; Fujiwara, C.; Yanase, I.; Takeda, H. Modification of Photoluminescence Wavelength and Decay Constant of Cr:$Gd_3Ga_5O_{12}$ Substituted by Ca/Si Cation Pair. *J. Ceram. Soc. Jpn.* **2024**, *132*, 364–368. [CrossRef]
24. Kitaura, M.; Zen, H.; Watanabe, S.; Masai, H.; Kamada, K.; Kim, K.J.; Ueda, J. Relationship between Ce^{3+} $5d_1$ Level, Conduction-Band Bottom, and Shallow Electron Trap Level in $Gd_3Ga_5O_{12}$:Ce and $Gd_3Al_1Ga_4O_{12}$:Ce Crystals Studied via Pump-Probe Absorption Spectroscopy. *Opt. Mater. X* **2025**, *25*, 100398. [CrossRef]
25. Petrenko, O.A.; Balakrishnan, G.; Paul, D.M.; Yethiraj, M.; McIntyre, G.J.; Wills, A.S. Field Induced Magnetic Order in the Frustrated Magnet Gadolinium Gallium Garnet. *J. Phys. Conf. Ser.* **2009**, *145*, 012026. [CrossRef]
26. Deen, P.P.; Florea, O.; Lhotel, E.; Jacobsen, H. Updating the Phase Diagram of the Archetypal Frustrated Magnet $Gd_3Ga_5O_{12}$. *Phys. Rev. B* **2015**, *91*, 014419. [CrossRef]
27. Sackville Hamilton, A.C.; Lampronti, G.I.; Rowley, S.E.; Dutton, S.E. Enhancement of the Magnetocaloric Effect Driven by Changes in the Crystal Structure of Al-Doped GGG, $Gd_3Ga_{5-x}Al_xO_{12}$ ($0 \leq x \leq 5$). *J. Phys. Condens. Matter* **2014**, *26*, 116001. [CrossRef]
28. Jin, X.; Zhao, J.; Gao, L.; Ma, H.; Oimod, H.; Zhu, H.; Li, Q.; Su, T.; Zhu, H.; Tegus, O.; et al. Influence of High-Pressure Heat Treatment on Magnetocaloric Effects and Magnetic Phase Transition in Single Crystal $Gd_3Ga_5O_{12}$. *J. Rare Earths* **2024**, *42*, 2112–2118. [CrossRef]
29. Chukalkin, Y.G.; Shtirts, V.R. Radiation Amorphization and Recovery of Crystal Structure in $Gd_3Ga_5O_{12}$ Single Crystals. *Phys. Status Solidi A* **1994**, *144*, 9–14. [CrossRef]

30. Mironova-Ulmane, N.; Sildos, I.; Vasil'chenko, E.; Chikvaidze, G.; Skvortsova, V.; Kareiva, A.; Muñoz-Santiuste, J.E.; Pareja, R.; Elsts, E.; Popov, A.I. Optical Absorption and Raman Studies of Neutron-Irradiated $Gd_3Ga_5O_{12}$ Single Crystals. *Nucl. Instrum. Methods Phys. Res. B* **2018**, *435*, 306–312. [CrossRef]
31. Potera, P.; Matkovskii, A.; Sugak, D.; Grigorjeva, L.; Millers, D.; Pankratov, V. Transient Color Centers in GGG Crystals. *Radiat. Eff. Defects Solids* **2002**, *157*, 709–713. [CrossRef]
32. Potera, P.; Ubizskii, S.; Sugak, D.; Schwartz, K. Induced Absorption in Gadolinium Gallium Garnet Irradiated by High-Energy ^{235}U Ions. *Acta Phys. Pol. A* **2010**, *117*, 181–183. [CrossRef]
33. Karipbayev, Z.T.; Kumarbekov, K.; Manika, I.; Dauletbekova, A.; Kozlovskiy, A.L.; Sugak, D.; Ubizskii, S.B.; Akilbekov, A.; Suchikova, Y.; Popov, A.I. Optical, Structural, and Mechanical Properties of $Gd_3Ga_5O_{12}$ Single Crystals Irradiated with $84Kr^+$ Ions. *Phys. Status Solidi B* **2022**, *259*, 2100415. [CrossRef]
34. Meftah, A.; Costantini, J.M.; Khalfaoui, N.; Boudjadar, S.; Stoquert, J.P.; Studer, F.; Toulemonde, M. Experimental Determination of Track Cross-Section in $Gd_3Ga_5O_{12}$ and Comparison to the Inelastic Thermal Spike Model Applied to Several Materials. *Nucl. Instrum. Methods Phys. Res. B* **2005**, *237*, 563–574. [CrossRef]
35. Toulemonde, M.; Meftah, A.; Costantini, J.M.; Schwartz, K.; Trautmann, C. Out-of-Plane Swelling of Gadolinium Gallium Garnet Induced by Swift Heavy Ions. *Nucl. Instrum. Methods Phys. Res. B* **1998**, *146*, 426–430. [CrossRef]
36. Meftah, A.; Assmann, W.; Khalfaoui, N.; Stoquert, J.P.; Studer, F.; Toulemonde, M.; Trautmann, C.; Voss, K.-O. Electronic Sputtering of $Gd_3Ga_5O_{12}$ and $Y_3Fe_5O_{12}$ Garnets: Yield, Stoichiometry and Comparison to Track Formation. *Nucl. Instrum. Methods Phys. Res. B* **2011**, *269*, 955–958. [CrossRef]
37. Costantini, J.-M.; Miro, S.; Beuneu, F.; Toulemonde, M. Swift Heavy Ion-Beam Induced Amorphization and Recrystallization of Yttrium Iron Garnet. *J. Phys. Condens. Matter* **2015**, *27*, 496001. [CrossRef]
38. Costantini, J.-M.; Miro, S.; Lelong, G.; Guillaumet, M.; Toulemonde, M. Damage Induced in Garnets by Heavy-Ion Irradiations: A Study by Optical Spectroscopies. *Philos. Mag.* **2018**, *98*, 312–328. [CrossRef]
39. Ozaki, N.; Nellis, W.J.; Mashimo, T.; Ramzan, M.; Ahuja, R.; Kaewmaraya, T.; Kimura, T.; Knudson, M.; Miyanishi, K.; Sakawa, Y.; et al. Dynamic Compression of Dense Oxide ($Gd_3Ga_5O_{12}$) from 0.4 to 2.6 TPa: Universal Hugoniot of Fluid Metals. *Sci. Rep.* **2016**, *6*, 26000. [CrossRef]
40. Khanin, V.M.; Rodnyi, P.A.; Wieczorek, H.; Ronda, C.R. Electron Traps in $Gd_3Ga_3Al_2O_{12}$:Ce Garnets Doped with Rare-Earth Ions. *Tech. Phys. Lett.* **2017**, *43*, 439–442. [CrossRef]
41. Lisiecki, R.; Komar, J.; Macalik, B.; Strzęp, A.; Berkowski, M.; Ryba-Romanowski, W. Exploring the Impact of Structure-Sensitive Factors on Luminescence and Absorption of Trivalent Rare Earth Embedded in Disordered Crystal Structures of $Gd_3Ga_5O_{12}$-$Gd_3Al_5O_{12}$ and Lu_2SiO_5-Gd_2SiO_5 Solid Solution Crystals. *Low Temp. Phys.* **2023**, *49*, 310–315. [CrossRef]
42. Karipbayev, Z.T.; Aralbayeva, G.M.; Zhalgas, A.T.; Burkanova, K.; Zhunusbekov, A.M.; Manika, I.; Akilbekov, A.; Bakytkyzy, A.; Ubizskii, S.; Sagyndykova, G.E.; et al. Radiation-Induced Disorder and Lattice Relaxation in $Gd_3Ga_5O_{12}$ Under Swift Xe Ion Irradiation. *Crystals* **2025**, *15*, 1065. [CrossRef]
43. Zorenko, Y.; Zorenko, T.; Voznyak, T.; Mandowski, A.; Xia, Q.; Batentschuk, M.; Friedrich, J. Luminescence of F^+ and F centers in Al_2O_3-Y_2O_3 oxide compounds. *IOP Conf. Ser. Mater. Sci. Eng.* **2010**, *15*, 012060. [CrossRef]
44. Babin, V.; Laguta, V.V.; Maaroos, A.; Makhov, A.; Nikl, M.; Zazubovich, S. Luminescence of F^+-type centers in undoped $Lu_3Al_5O_{12}$ single crystals. *Phys. Status Solidi B* **2011**, *248*, 845–852. [CrossRef]
45. Varney, C.R.; Selim, F.A. Color centers in YAG. *AIMS Mater. Sci.* **2015**, *2*, 560–572. [CrossRef]
46. Pankratova, V.; Skuratov, V.A.; Buzanov, O.A.; Mololkin, A.A.; Kozlova, A.P.; Kotlov, A.; Popov, A.I.; Pankratov, V. Radiation effects in $Gd_3(Al,Ga)_5O_{12}$:Ce^{3+} single crystals induced by swift heavy ions. *Opt. Mater. X* **2022**, *16*, 100217. [CrossRef]
47. Pankratova, V.; Butikova, J.; Kotlov, A.; Popov, A.I.; Pankratov, V. Influence of swift heavy ions irradiation on optical and luminescence properties of $Y_3Al_5O_{12}$ single crystals. *Opt. Mater. X* **2024**, *23*, 100341. [CrossRef]
48. Song, Y.; Song, J.; Qiu, M.; Wang, G.; Zhang, J. Temperature and fluence dependence of the luminescence properties of Ce:YAG single crystals with ion beam-induced luminescence. *Radiat. Meas.* **2023**, *160*, 106878. [CrossRef]
49. Assylbayev, R.; Lushchik, A.; Lushchik, C.; Kudryavtseva, I.; Shablonin, E.; Vasil'chenko, E.; Akilbekov, A.; Zdorovets, M. Structural defects caused by swift ions in fluorite single crystals. *Opt. Mater.* **2018**, *75*, 196–203. [CrossRef]
50. Assylbayev, R.; Akilbekov, A.; Dauletbekova, A.; Lushchik, A.; Shablonin, E.; Vasil'chenko, E. Radiation damage caused by swift heavy ions in CaF_2 single crystals. *Radiat. Meas.* **2016**, *90*, 18–22. [CrossRef]
51. Baubekova, G.; Assylbayev, R.; Feldbach, E.; Krasnikov, A.; Kudryavtseva, I.; Podelinska, A.; Seeman, V.; Shablonin, E.; Vasil'chenko, E.; Lushchik, A. Accumulation of oxygen interstitial-vacancy pairs under irradiation of corundum single crystals with energetic xenon ions. *Radiat. Meas.* **2024**, *179*, 107324. [CrossRef]
52. Assylbayev, R.; Akilbekov, A.; Baubekova, G.; Chernenko, K.; Zdorovetz, M.; Feldbach, E.; Shablonin, E.; Lushchik, A. Defect-related luminescence of MgO single crystals irradiated with swift ^{132}Xe ions. *Opt. Mater.* **2022**, *127*, 112308. [CrossRef]

53. Assylbayev, R.; Tursumbayeva, G.; Baubekova, G.; Karipbayev, Z.T.; Krasnikov, A.; Shablonin, E.; Aralbayeva, G.M.; Smortsova, Y.; Akilbekov, A.; Popov, A.I.; et al. Influence of Energetic Xe^{132} Ion Irradiation on Optical, Luminescent and Structural Properties of Ce-Doped $Y_3Al_5O_{12}$ Single Crystals. *Crystals* **2025**, *15*, 683. [CrossRef]
54. Uglov, V.V.; Kholad, V.M.; Grinchuk, P.S.; Ivanov, I.A.; Kozlovsky, A.L.; Zdorovets, M.V. Study of the Microstructure and Phase Composition of Ceramics Based on Silicon Carbide Irradiated with Low-Energy Helium Ions. *Inorg. Mater. Appl. Res.* **2024**, *15*, 591–595. [CrossRef]
55. Ryskulov, A.E.; Ivanov, I.A.; Kozlovskiy, A.L.; Konuhova, M. The effect of residual mechanical stresses and vacancy defects on the diffusion expansion of the damaged layer during irradiation of BeO ceramics. *Opt. Mater. X* **2024**, *24*, 100375. [CrossRef]
56. Kruglyakov, M.A.; Kudiiarov, V.N.; Laptev, R.S.; Vrublevskii, D.B.; Svyatkin, L.A.; Uglov, V.V.; Ivanov, I.A.; Koloberdin, M.V. Influence of Chromium Coating on Microstructure Changes in Zirconium Alloy E110 Under High-Temperature Hydrogenation and Kr Ion Irradiation. *Coatings* **2025**, *15*, 133. [CrossRef]
57. Staltsov, M.S.; Chernov, I.I.; Emelyanova, O.V.; Khmelenin, D.N.; Dikov, A.S.; Ivanov, I.A. Microstructure evolution of 18Cr10Ni-Ti-modified steel after heavy ions irradiation. *J. Mater. Sci.* **2026**, *61*, 1261–1279. [CrossRef]
58. Eugene, K.A.; Assylbayev, R.; Baubekova, G.; Kudryavtseva, I.; Kuzovkov, V.N.; Podelinska, A.; Seeman, V.; Shablonin, E.; Lushchik, A. Annealing of Oxygen-Related Frenkel Defects in Corundum Single Crystals Irradiated with Energetic Xenon Ions. *Crystals* **2025**, *15*, 573. [CrossRef]
59. Maji, S.B.; Vanetsev, A.; Mändar, H.; Nagirnyi, V.; Chernenko, K.; Kirm, M. Investigation of Luminescence Properties of Hydrothermally Synthesized Pr^{3+} Doped $BaLuF_5$ Nanoparticles under Excitation by VUV Photons. *Opt. Mater.* **2024**, *154*, 115781. [CrossRef]
60. Krutyak, N.; Nagirnyi, V.; Romet, I.; Deyneko, D.; Spassky, D. Energy Transfer Processes in NASICON-Type Phosphates under Synchrotron Radiation Excitation. *Symmetry* **2023**, *15*, 749. [CrossRef]
61. Spassky, D.; Voznyak-Levushkina, V.; Arapova, A.; Zadneprovski, B.; Chernenko, K.; Nagirnyi, V. Enhancement of Light Output in $Sc_xY_{1-x}PO_4:Eu^{3+}$ Solid Solutions. *Symmetry* **2020**, *12*, 946. [CrossRef]
62. Romet, I.; Tichy-Rács, É.; Lengyel, K.; Feldbach, E.; Kovács, L.; Corradi, G.; Chernenko, K.; Kirm, M.; Spassky, D.; Nagirnyi, V. Interconfigurational d-f Luminescence of Pr^{3+} Ions in Praseodymium Doped $Li_6Y(BO_3)_3$ Single Crystals. *J. Lumin.* **2024**, *265*, 120216. [CrossRef]
63. Bartosiewicz, K.; Szysiak, A.; Tomala, R.; Gołębiewski, P.; Węglarz, H.; Nagirnyi, V.; Kirm, M.; Romet, I.; Buryi, M.; Jary, V.; et al. Energy-Transfer Processes in Nonstoichiometric and Stoichiometric Er^{3+}, Ho^{3+}, Nd^{3+}, Pr^{3+}, and Cr^{3+}-Codoped Ce:YAG Transparent Ceramics: Toward High-Power and Warm-White Laser Diodes and LEDs. *Phys. Rev. Appl.* **2023**, *20*, 014047. [CrossRef]
64. Gundacker, S.; Pots, R.H.; Nepomnyashchikh, A.; Radzhabov, E.; Shendrik, R.; Omelkov, S.; Kirm, M.; Acerbi, F.; Capasso, M.; Paternoster, G.; et al. Vacuum Ultraviolet Silicon Photomultipliers Applied to BaF_2 Cross Luminescence Detection for High Rate Ultrafast Timing Applications. *Phys. Med. Biol.* **2021**, *66*, 114002. [CrossRef]
65. Saaring, J.; Feldbach, E.; Nagirnyi, V.; Omelkov, S.; Vanetsev, A.; Kirm, M. Ultrafast Radiative Relaxation Processes in Multication Cross Luminescence Materials. *IEEE Trans. Nucl. Sci.* **2020**, *67*, 1009–1013. [CrossRef]
66. Smortsova, Y.; Chukova, O.; Kirm, M.; Nagirnyi, V.; Pankratov, V.; Kataev, A.; Kotlov, A. The P66 time-resolved VUV spectroscopy beamline at PETRA III storage ring of DESY. *J. Synchrotron Rad.* **2025**, *32*, 1539–1548. [CrossRef] [PubMed]
67. Papagelis, K.; Arvanitidis, J.; Vinga, E.; Christofilos, D.; Kourouklis, G.A.; Kimura, H.; Ves, S. Vibrational properties of solid solutions. *J. Appl. Phys.* **2010**, *107*, 113504. [CrossRef]
68. Li, H.; Sun, D.; Zhang, H.; Luo, J.; Quan, C.; Qiao, Y.; Dong, K.; Chen, Y.; Wang, Z.; Cheng, M.; et al. Growth, Rietveld Refinement, Raman Spectrum and Dislocation of Ca/Mg/Zr-Substituted GGG: A Potential Substrate and Laser Host Material. *J. Mater. Sci. Mater. Electron.* **2024**, *35*, 12777. [CrossRef]
69. Syvorotka, I.I.; Sugak, D.; Yakhnevych, U.; Buryy, O.; Włodarczyk, D.; Pieniążek, A.; Zhydachevskyy, Y.; Levintant-Zayonts, N.; Savytskyy, H.; Bonchyk, O.; et al. Investigation of the Interface of $Y_3Fe_5O_{12}/Gd_3Ga_5O_{12}$ Structure Obtained by the Liquid Phase Epitaxy. *Cryst. Res. Technol.* **2022**, *57*, 2100180. [CrossRef]
70. Varney, C.R.; Reda, S.M.; Mackay, D.T.; Rowe, M.C.; Selim, F.A. Strong Visible and Near-Infrared Luminescence in Undoped YAG Single Crystals. *AIP Adv.* **2011**, *1*, 042170. [CrossRef]
71. Matkovskii, A.; Sugak, D.; Melnyk, S.; Potera, P.; Suchocki, A.; Frukacz, Z. Colour Centers in Doped $Gd_3Ga_5O_{12}$ and $Y_3Al_5O_{12}$ Laser Crystals. *J. Alloys Compd.* **2000**, *300–301*, 395–397. [CrossRef]
72. Andriichuk, V.A.; Volzhenskaya, L.G.; Zakharko, Y.M.; Zorenko, Y.V. Influence of structure defects upon the luminescence and thermostimulated effects in $Gd_3Ga_5O_{12}$ crystals. *J. Appl. Spectrosc.* **1987**, *47*, 902–905. [CrossRef]
73. Aralbayeva, G.; Karipbayev, Z.; Zafari, U.; Bakytkyzy, A.; Zhunusbekov, A.; Kumarbekov, K.; Popov, A.I. Modeling Defect States and the Role of 4f Electrons in $Gd_3Ga_5O_{12}$ Using DFT Methods. *Bull. L.N. Gumilyov Eurasian Natl. Univ. Phys. Astron. Ser.* **2025**, *152*, 169–187. [CrossRef]

74. Shirinyan, A.; Bilogorodskyy, Y. Effect of radiation-induced vacancy saturation on the first-order phase transformation in nanoparticles: Insights from a model. *Beilstein J. Nanotechnol.* **2024**, *15*, 1453–1472. [CrossRef]
75. Kotomin, E.; Kuzovkov, V. Radiation-induced aggregatization of immobile defects. *Solid State Commun.* **1981**, *39*, 351–354. [CrossRef]
76. Kuzovkov, V.N.; Kotomin, E.A. The kinetics of defect accumulation under irradiation: Many-particle effects. *Phys. Scr.* **1993**, *47*, 585. [CrossRef]
77. Sibley, W.A. Radiation processes in halide crystals and glasses. *Nucl. Instrum. Methods Phys. Res. B* **1988**, *32*, 194–200. [CrossRef]
78. Sonder, E.; Sibley, W.A.; Rowe, J.E.; Nelson, C.M. Some properties of defects produced by ionizing radiation in KCl between 80 and 300° K. *Phys. Rev.* **1967**, *153*, 1000. [CrossRef]
79. Lushchik, A.; Podelinska, A.; Seeman, V.; Shablonin, E.; Kotomin, E.A.; Kuzovkov, V.N. Open questions on the thermal stability of primary electronic centers in irradiated MgO single crystals. *J. Phys. Chem. C* **2025**, *129*, 2775–2781. [CrossRef]
80. Logan, J.V.; Webster, P.T.; Woller, K.B.; Morath, C.P.; Short, M.P. Understanding the fundamental driver of semiconductor radiation tolerance with experiment and theory. *Phys. Rev. Mater.* **2022**, *6*, 084601. [CrossRef]